BOLETIN DE LA SOCIEDAD ESPAÑOLA DE
Cerámica y Vidrio
www.elsevier.es/bsecv

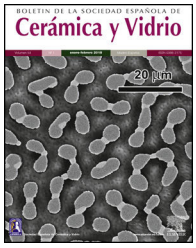

Effect of Ta2O5 content on the microstructural properties of 45S5 bioglass glass-ceramic scaffolds

Cindy Sinaí Veláquez-González, Ena Athenea Aguilar-Reyes, Carlos Alberto León-Patiño*

Instituto de Investigación en Metalurgia y Materiales, Universidad Michoacana de San Nicolás de Hidalgo, Morelia, Mich., Mexico

ARTICLE INFO

Article history:
Received 8 December 2023
Accepted 25 April 2024
Available online 17 May 2024

Keywords:
Tantalum oxide
45S5 bioglass
Scaffolds
Microstructure
Porosity

ABSTRACT

Bioactive glasses are mainly used to repair bone defects since they stimulate the natural healing of damaged tissues, allowing the adhesion and proliferation of bone-forming cells. On the other hand, tantalum is known to have good chemical resistance and biocompatibility, with no adverse biological response in organisms. In the present work, 45S5 bioglass systems undoped and doped with Ta_2O_5 were prepared according to the following stoichiometric molar relationship $(46-x)SiO_2-26.9CaO-24.4Na_2O-2.6P_2O_5-xTa_2O_5$ ($x=0$, 0.1, 0.5) by the conventional melt quenching technique. Subsequently, scaffolds from these glassy systems were prepared using the combined method of powder technology and polymer foaming. Both, glass powders and scaffolds, were physicochemical characterized. The results showed that the 0.5 mol% Ta_2O_5-doped scaffolds exhibited less contraction (36.53%) and higher porosity (84.24%) during sintering, with interconnected porosity, pore size in the range of 19–260 μm, and a greater surface area ($17.431\pm0.846\ m^2/g$) than the scaffolds with no Ta_2O_5. Furthermore, the tantalum oxide promoted the formation of a sodium tantalum phosphate phase, along with the combeite and silicorhenanite present in the undoped-glass scaffolds. The maximum compressive strength of scaffolds ranged from 0.42 to 1.40 MPa and the elastic modulus (*E*) from 0.19 to 0.47 GPa.

Efecto del contenido de Ta_2O_5 en las propiedades microestructurales de andamios vitrocerámicos de biovidrio 45S5

Palabras clave:
Óxido de tantalio
Biovidrio 45S5
Andamios
Microestructura
Porosidad

RESUMEN

Los vidrios bioactivos se usan principalmente para reparar defectos óseos ya que pueden estimular la curación natural de los tejidos dañados permitiendo la adhesión y proliferación de las células formadoras de hueso. Por otro lado, se sabe que el tantalio posee buena resistencia química, biocompatibilidad, sin respuestas biológicas adversas en los organismos. En el presente trabajo, se prepararon sistemas de biovidrio 45S5 sin dopar y

* *Corresponding author.*
E-mail address: ena.aguilar@umich.mx (E.A. Aguilar-Reyes).
https://doi.org/10.1016/j.bsecv.2024.04.004

dopados con Ta_2O_5 de acuerdo con la siguiente relación molar estequiométrica (46-x)SiO_2-26,9 CaO-24,4Na_2O-2,6P_2O_5-xTa_2O_5 (x = 0, 0,1, 0,5) mediante la técnica convencional de fusión y temple. Posteriormente, se prepararon andamios a partir de estos sistemas vítreos utilizando el método combinado de tecnología de polvos y espumado de polímeros. Tanto los polvos como los andamios de biovidrio fueron caracterizados fisicoquímicamente. Los resultados mostraron que los andamios dopados con 0,5 mol% Ta_2O_5 presentaron menos contracción (36,53%) y más alta porosidad (84,24%) durante la sinterización, con porosidad interconectada, tamaño de poro en el rango de 19-260 μm, y una mayor área superficial (17,431 ± 0,846 m^2/g) que los andamios sin Ta_2O_5. Además, la adición de óxido de tantalio promovió la formación de la fase de fosfato de tantalio y sodio, junto con la combeita y la silicorhenanita presentes en los andamios sin dopar. La máxima resistencia a la compresión de los andamios varió entre 0,42 y 1,40 MPa y el módulo de elasticidad (E) entre 0,19 y 0,47 GPa.

Introduction

A silica-based glass is formed by tetrahedra in a sodium–calcium–silica system (Na_2O–CaO–SiO_2) and is resistant to different chemical environments. Specific glasses can be active in the body and stimulate the natural healing of damaged tissues, mainly in defects around the host bone. Their degradation upon implantation is essential because the stimulation of osteoprogenitor cells that differentiate into osteoblasts (osteoinduction) and the space for new tissue growth depends on their dissolution [1].

Impurities and network modifiers can influence the mechanical and chemical properties of the glass, and depending on the ions used, their functionality such as Ag ions for antibacterial use [2], Ca ions to accelerate blood coagulation [3], Eu ions to stimulate bone formation in vitro and in vivo in rats [4], Ga ions as possible hemostatic agents and antibacterial properties [5], etc.

Tantalum (Ta) forms a thin oxide film on the surface of the metal that makes it impenetrable, which inhibits the access of harmful substances, including acids and alkalis. In medicine, Ta nanoparticles have been used as contrast agents for X-rays, for instance, increasing the radiopacity of bone cement [6], hydrogel compounds [7], etc. Ta, compared to titanium, has a higher density of living cells on the surface; its adhesion and cell growth promote the formation of an extracellular matrix [8], with 80% occupancy of new bone in pores [9]. Furthermore, Ta has proved to be bioactive and biocompatible, able to form apatite on its surface upon immersion in simulated body fluid [10].

For its part, Ta_2O_5 is part of the refractory metal oxides, which, when combined with other oxides, can form glass. Mendoca et al. [11] employed Ta-doped bioglass to improve clotting time in hemostatic clips; Ta_2O_5 powder has also been deposited on gauze to prevent bacterial infections and accelerate blood clotting [12].

Scaffolds are temporary, biodegradable, and biocompatible three-dimensional structures to which cells can adhere and differentiate to create new bone tissue. When manufacturing them, the technique that allows controlling the topography and roughness of the surface, as well as the size and interconnection of the pores, must be considered to enable migration and adhesion on the surface [13]. Scaffolds have been designed from biopolymers such as alginate, collagen, and chitosan [14] and bioceramics such as calcium phosphate, hydroxyapatite, and bioglass [15]. Several authors have incorporated metal ions into the bioactive glass to functionalize scaffolds and promote the differentiation of cells that stimulate the formation of bone tissue. Míguez-Pacheco et al. [16] incorporated Li into the glass composition and fabricated scaffolds with 90% interconnected porosity that enhanced osteoblast cell activity. Li et al. [17] included Co by extrusion in 3D printed structures, with 40% interconnected porosity in 500 μm pores and increased osteogenic and angiogenic activity. Also, Zhao et al. [18] used the hydrothermal method to fabricate bioceramic scaffolds doped with Sr with 80% porosity, which delayed the bone loss induced by osteoporosis. Du et al. [19] prepared calcium silicate scaffolds doped with Mg and Mn, with a porosity of 57%, that promoted osteogenic differentiation of the mesenchymal stroma of bone marrow.

In the present work, 45S5 bioglass was doped with tantalum oxide at two different compositions, 0.1 and 0.5 mol%, to produce 3D scaffolds by the combined method of powder technology and polymer foaming to evaluate its effect on the physicochemical, microstructural, and mechanical properties that can affect their performance in future studies of bioactivity in biological medium and biocompatibility with osteoprogenitor cells. Although studies have already been carried out on bioactive glasses and glass-ceramics with the addition of different ions for therapeutic purposes, this is the first time that the effect of Ta_2O_5 on the microstructure of bioglasses and bioglass scaffolds derived from 45S5 has been studied.

Experimental

Glass network connectivity

The network connectivity (NC) of an inorganic glass, that is, the number of bridging oxygens (BO) per tetrahedron $[SiO_4]^{4-}$,

is a measure of the degree of crosslinking and connectivity of the silica, and there is a supporting equation for predicting glass properties from composition, including bioactivity. The NC of bioglass formulations in this work were calculated using Eq. (1), considering SiO_2 and P_2O_5 as network formers, CaO and Na_2O as modifiers, and Ta_2O_5 as an intermediate. Intermediate oxides are network former (NC^1) or modifiers (NC^2) [1].

$$NC = 2 + \frac{(BO - NBO)}{G} \quad (1)$$

BO = number of bridging oxygens per network-forming ion.
NBO = number of non-bridging oxygens per network-modifier ion.
G = number of glass-forming units.

Bioactive glass preparation

Glasses were made by the conventional melt-quenching technique from a mixture of high-purity oxide and carbonate powders (SiO_2, CaO, Na_2CO_3, P_2O_5, and Ta_2O_5, ≥98%, Sigma–Aldrich); the powder was then placed in a fused silica crucible and heated at 900 °C for 90 min; subsequently, it was brought to 1350 °C for 90 min, in a Carbolite HTF 17/10 furnace. The molten mixture was quenched in water at room temperature (RT) to obtain a frit, then dried in a Thermo Scientific Lindberg Blue M vacuum oven for 24 h. Afterward, it was pulverized in a Retsch RS200 vibratory disk mill and sieved to a particle size of <63 μm; finally, powder was further ground in a planetary ball mill Restch PM400 at 200 RMP, and the particle size and its distribution were determined by a Horiba centrifugal automatic particle analyzer. The 45S5 bioglass undoped and doped with 0.1 mol% and 0.5 mol% of Ta_2O_5 were labeled as BG0, BG-0.1%Ta and BG-0.5%Ta, respectively.

Scaffolds preparation

The combined method of powder technology and polymer foaming was used to obtain the scaffolds, following the methodology reported by Aguilar-Reyes et al. [20] First, the glass powder was dry-mixed with a phenolic resin and a foaming agent (p-toluene-sulfonyl hydrazide, TSH 97%) in a ratio of 45:52:3 wt.%, respectively, in a conventional ball mill, the powder mixture was then placed into cylindrical stainless-steel molds. The molds were placed in a muffle for heat treatment; the resin was melted at 80 °C to form a suspension of TSH and glass particles; at 120 °C, the TSH decomposed, releasing gas, and expanding the suspension, and the temperature was further increased to 200 °C for the complete decomposition of the TSH. Finally, at 500 °C, the resin was burned out, and at 900 °C, the microporous bioglass structure was sintered for 1 h. The scaffolds of 45S5 bioglass undoped and doped with 0.1 mol% and 0.5 mol% of Ta_2O_5 were labeled as SBG0, SBG-0.1%Ta and SBG-0.5%Ta, respectively.

Characterization

Bioactive glass powders

The quantitative analyses of the prepared bioglass formulations were determined in a Rigaku WDXRF Primus II sequential X-ray Fluorescence (XRF) spectrometer; tantalum was analyzed in compressed powder using EZscan software, prepared and validated by Rigaku, for comparison. The glass powder densities were measured using the AccuPyc 1330 pycnometer. Values for reported density are the average of 5 measurements. The particle size was measured in a Horiba centrifugal automatic particle analyzer CAPA-300. The Barret–Emmett–Teller (BET) method was used to calculate the specific surface area (S_{BET}) in a Horiba Scientific SA-9600 series surface area analyzer. X-ray diffraction (XRD) patterns were recorded using a Bruker D8 Advance diffractometer using Cu-Kα radiation (λ = 1.541 Å) from 10 to 70° at a step size of 0.02°. A TA Instruments SDT Q600 simultaneous thermal analyzer was used to study the thermal behavior at a heating rate of 20 °C/min from RT to 1300 °C and argon atmosphere, using alumina crucibles. The Raman analysis was carried out using Raman Luminicent microscope equipment, Rammics M532, and an Olympus CX-41 microscope. Fourier Transform infrared spectroscopy (FTIR) spectra were recorded using a Bruker Tensor 27 FTIR spectrophotometer.

Scaffolds

The theoretical porosity and the surface area of scaffolds were determined from the apparent density of the foams (ρ_{app}), which was calculated from the mass and dimensions of the scaffolds, the theoretical density of 45S5 bioactive glass was taken as $\rho_{theo} = 2.7$ g/cm^3 [21]. Each reported value is an average of 6 measurements. The percentage of shrinkage of the scaffolds after heat treatment was calculated considering the volume before and after sintering. A Jeol-JSM 7600F field emission scanning electron microscope (SEM) was used to analyze the microstructure and porosity of the scaffolds. A copper coating was deposited on the sample's surface to improve the electrons' scattering. The pore size and pore size distribution in pure and Ta_2O_5-doped scaffolds (Feret diameter) were evaluated with the Nano measurer 1.2 software from micrographs taken at 100×. XRD analyses in the pulverized sintered scaffolds were used to determine the crystalline phases, and the measurements were carried out in the 2θ range 10–80° with increments of 0.02° at 0.6 s per step. The FTIR analyses were conducted to determine the vibration modes of the functional groups in the pulverized sintered scaffolds that were diluted in KBr before the spectrum recording. More detailed microstructural characterization of sintered scaffolds was obtained by transmission electron microscopy (TEM) (Jeol TEM JEM2010 FEG). Interplanar distances were calculated from the FFT patterns to identify the crystalline phases present in the sample. A Lloyd Instruments EZ Series EZ50 universal materials testing machine was used to measure the unconfined compressive strength of the scaffolds from cylindrical specimens of approximately 23 mm in height by 15 mm in diameter, with a 5 KN preload cell. The crosshead speed was 100 mm/min. The compressive strength was defined as the

Table 1 – Nomenclature, composition in mol% (wt.%), and network connectivity values of glassy systems.

Nomenclature	SiO_2	CaO	Na_2O	P_2O_5	Ta_2O_5	NC^1	NC^2
BG0	46.1 (45)	26.9 (24.5)	24.4 (24.5)	2.6 (6.0)	--	1.90	1.90
BG-0.1%Ta	46 (44.6)	26.9 (24.3)	24.4 (24.4)	2.6 (6.0)	0.1 (0.7)	1.90	1.89
BG-0.5%Ta	45.6 (43.1)	26.9 (23.8)	24.4 (23.8)	2.6 (5.8)	0.5 (3.5)	1.90	1.86

maximum on the stress-strain curves, reporting the average compressive strength of six specimens for each glass formulation.

Results and discussion

Determination of glass network connectivity

The NC provides the degree of crosslinking of the glass and, in turn, estimates whether the formulation can promote the bioactivity of glass in the body. Tilocca et al. [22] reported that in the glass formation process, P_2O_5 in amounts of 2–5 mol% forms PO_4 groups that are incorporated into the glass network, giving rise to Si—O—P or P—O bonds, which are isolated as orthophosphates, and act as glass formers in the Si lattice. For this reason, in the bioglass formulations, P_2O_5 was considered a network-former, and Ta_2O_5 was considered both a network-former and a modifier.

The calculated NCs are shown in Table 1; values of 1.90 were calculated for all compositions in which Ta_2O_5 is considered as a former in the SiO_2 network (NC^1); in contrast, the values are reduced as the percentage of tantalum oxide increases if it is regarded as a modifier of the network (NC^2). If Ta_2O_5 acts as a modifier of the SiO_2 network, the probability of rapid dissolution when immersed in SBF increases. Glasses with NC greater than 2.4 are not likely to be bioactive since the energy barrier for crystallization is more significant due to the stabilizing effect of the crosslinking of the silicate chains [1]. It should be noted that glasses with NC values greater than 2.4 slow down new bone formation, increasing tissue regeneration time. In contrast, glasses with NC values less than 1.8 increase the material's solubility and could fragment the scaffold structure. De Siqueira et al. [23] concluded, based on the cell viability results, that Nb behaves as a network modifier when the composition is 1.2 mol% with an NC = 1.77, observing more significant proliferation of the MG63 cell line; on the other hand, it acts as a network former at concentrations of 2.5 mol% with an NC = 2.34, reducing the viability of the lineage. With the results obtained from NC, it is expected that the degradability and biological response of the material will allow tissue regeneration in the different bioglass formulations.

Bioactive glass characterization

The chemical composition of the different bioactive glass formulations determined by XRF is very close to those stated by stoichiometry, with a slight increase in the SiO_2 content; this increase is due to the minor dissolution of the fused silica crucible used to melt the mixture of oxides. The Ta_2O_5 content was 0.73 and 3.18 wt.%, corresponding to 0.1 and 0.5 mol% of Ta_2O_5 added to the formulations. The presence of other oxides as impurities, such as MgO, K_2O, Al_2O_3, Fe_2O_3, TiO_2, and MnO, was also detected by XRF and equivalent to 2.3–2.6 wt.%.

The density, particle size, and specific surface area of each bioglass formulation are reported in Table 2. It is noted that the density of BG0 (2.7117 g/cm^3) agreed well with that reported by Sepulveda et al. [21] and O'Donnell et al. [24], and it is greater than those of the formulations containing Ta_2O_5. As the molar proportion of Ta_2O_5 increases, the density decreases, with BG-0.5%Ta being the formulation with the lowest density. Also, it can be observed that there is a greater surface area in the BG-0.5%Ta formulation with 0.5649 m^2/g, which agrees with the results obtained in the particle size analysis since this formulation has the smallest particle size compared to the other formulations and consequently higher surface reactivity, which would promote the growth of hydroxyapatite on the surface [25].

The differential scanning calorimetry (DSC) curves with the thermal events recorded for the formulated glasses are shown in Fig. 1. The glass transition temperatures (T_g) were found to be 562.7 °C, 562.9 °C and 566.3 °C for BG0, BG-0.1%Ta and BG-0.5%Ta samples, respectively, which increases as the Ta_2O_5 content increases. Various authors have reported that the incorporation of transition metals, such as Ta, in glasses increases T_g; this incorporation process requires higher temperatures to relax the glass structure, which is associated with the presence of ionic bonds of Ta—O in orthorhombic form that cross the network; since they are stronger than Si—O—Si or P—O—P bonds and thus facilitates the incorporation of the transition metal oxide into the glass network [26]. The silicon (Si^{4+}) can generate four binding sites while tantalum (Ta^{5+}) generates 5, so it is considered a crosslinking site in the lattice, which reduces the mobility of the glass chains. Since the net relaxation temperature is influenced by the bonding of the atoms, the greater the amount of tantalum oxide, the more energy is required to relax the lattice chains. After the glass transition, the crystallization temperature (T_c) is found, where BG-0.1%Ta shows a higher exothermic peak of 783.3 °C concerning BG0 where crystallization occurs at 778.7 °C due to the increase in the amount of energy that requires the formulation to order the crystalline phases. In comparison, in BG-0.5%Ta, the exothermic event occurs at 775.9 °C, so the T_c of the material is reached more quickly than in the other formulations. Finally, the melting temperature (T_m) is presented at 1176 °C, 1193 °C and 1171.6 °C for BG0, BG-0.1%Ta, and BG-0.5%Ta, respectively; this last endothermic reaction indicates the slow melting of some glass elements present in BG-0.1%Ta, which may reveal the presence of a more complex crystalline structure of the material concerning the BG0 and that in the BG-0.5%Ta formulation.

Some authors have analyzed the crystallization of bioglasses since this influences the mechanical properties of the scaffolds, and, in turn, there are crystalline phases that could

Table 2 – Density, particle size and specific surface area for the glass powders.

Sample	Density (g/cm^3)	Particle size (μm)	S_{BET} (m^2/g)
BG0	2.7117 ± 0.0012	3.51 ± 0.94	0.4052
BG-0.1%Ta	2.6614 ± 0.0013	3.25 ± 0.82	0.4099
BG-0.5%Ta	2.6463 ± 0.0009	2.87 ± 0.97	0.5649

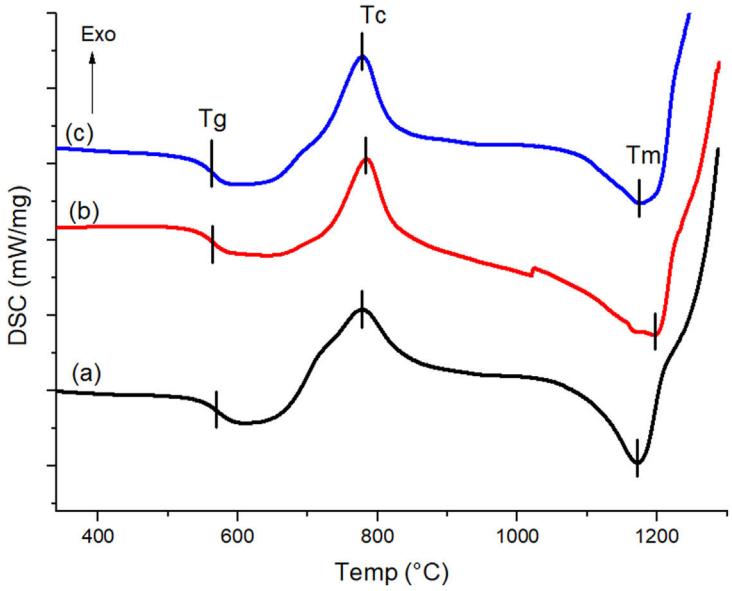

Fig. 1 – DSC curves for the glassy systems: (a) BG0, (b) BG-0.1%Ta, and (c) BG-0.5%Ta.

Table 3 – Characteristic temperatures and ΔT, K_H and K_W values estimated for (46 − x) SiO_2–26.9 CaO–24.4Na_2O–2.6P_2O_5–xTa_2O_5 (x = 0, 0.1, 0.5 mol%) glassy systems.

Bioglass	T_g (°C)	T_x (°C)	T_c (°C)	T_m (°C)	ΔT (°C)	K_H	K_W
BG0	562.7	620	778.7	1176	57.3	0.144	0.049
BG-0.1%Ta	562.9	656	783.3	1193	93.1	0.227	0.078
BG-0.5%Ta	566.3	626	775.9	1171.6	59.7	0.151	0.051

be detrimental to the bioactivity of the material [27,28]. For this reason, the thermal behavior of powdered glasses was analyzed to predict the crystalline phases, the glass stability, and the change in the T_c of the compositions and to predict its effect on the bioactivity of the scaffold. Table 3 summarizes the characteristic glass temperatures such as T_g, onset crystallization temperature (T_x), maximum of the T_c, and T_m. Based on the results obtained, the thermal stability and glass-forming ability of the glasses under study were evaluated using various thermal stability criteria (Dietzel factor, Hruby parameter, and Weinberg parameter) [26,28].

Dietzel factor:

$$\Delta T = T_x - T_g \tag{2}$$

Hruby parameter:

$$K_H = \frac{T_x - T_g}{T_m - T_c} \tag{3}$$

Weinberg parameter:

$$K_W = \frac{T_x - T_g}{T_m} \tag{4}$$

The results obtained from the thermal analysis are influenced by the presence of Ta_2O_5 and the non-bridging oxygens (NBO) present in the glass network; on the other hand, the ΔT of glasses should not exceed 100 °C since glasses with higher values present a compact structure, which might slow down the bioactivity of the material in a biological environment. Table 3 shows that the ΔT values of glassy systems are less than 100 °C, so they are considered feasible for bioactivity analysis. The K_H obtained is less than 0.5, which suggests that glasses have good thermal stability and present crystallization and nucleation processes [27]. The K_W indicates that the BG-0.1%Ta devitrification occurs more slowly than the other formulations [28].

To better understand the thermal behavior observed in DSC, Raman analysis was performed to determine the anionic structure and dynamics of the formulations. Fig. 2 depicts a comparison of Raman spectra for the glassy systems; the predominant bands in the three spectra are located: the band at

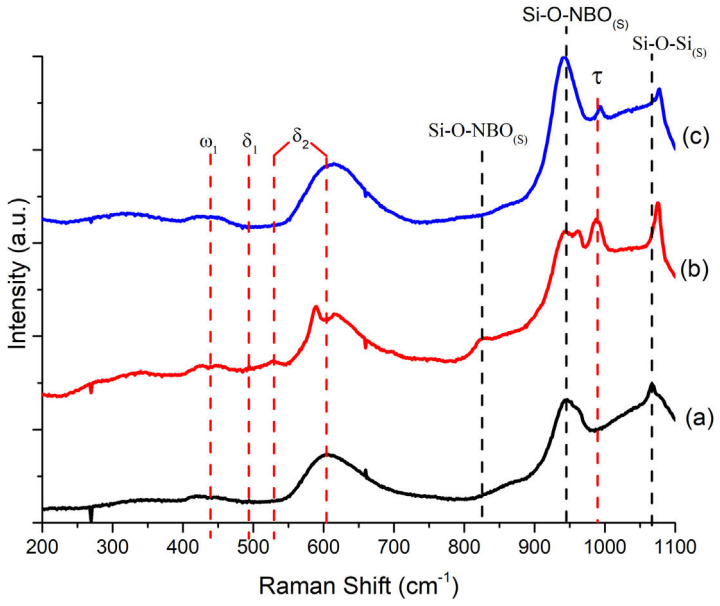

Fig. 2 – Raman spectra of glassy systems, (a) BG0, (b) BG-0.1%Ta and (c) BG-0.5%Ta.

438 cm^{-1} corresponds to ω_1 (>5 rings linking the glass tetrahedron structure), at 494 cm^{-1} δ_1 (4-membered rings) is detected, and both bands at 530 cm^{-1} and 610 cm^{-1} correspond to δ_2 (3-membered rings) which are attributed to the equilibrium of BO bonds in structural units containing NBO and Si—O—Si bonds in rings of silanol units [29]; the band at 945 cm^{-1} is associated with the metasilicate unit $[Si_2O_6]^{4-}$ of the $_{Si}Q^2$ species in the vitreous structure, where the tetrahedron of the silicon structure is shared (Si—NBO) [29,30]; and the band at 1066 cm^{-1} corresponds to the asymmetric stretching of the BO in all Q species. It should be noted that as the amount of Ta_2O_5 increases, there is a slight band shift, and its intensity weakens since its incorporation influences the arrangement of P in the glass lattice [31]. With the incorporation of Ta_2O_5, an 825 cm^{-1} band weakens in intensity as the amount of dopant increases. It is suggested that the incorporation of Ta_2O_5 breaks the silicate chains and modifies the reticular structure into a new one of orthorhombic Ta—O chains that share its vertices; this, in turn, influences the increase in T_c and T_m in BG-0.1%Ta to reduce the mobility of the chains; this behavior has been reported for phosphosilicates, borosilicates, and other glasses with alkaline and alkaline earth oxides [31]. The band that is observed at 993 cm^{-1} expressed only in the formulations with Ta_2O_5 but decreased in BG-0.5%Ta indicating the entry of tantalum as a network former between silicon and phosphorus since the latter is expressed at 430 cm^{-1} PO_4^{-3}(s), 946 cm^{-1} PO_4^{-3}(st) and 1030 cm^{-1} PO_4^{-3}(as) [31], forming the crystalline structure with lower energy.

The diffraction pattern for the formulated glass powders doped with Ta_2O_5 presented in Fig. 3(a) confirmed their amorphous nature, with no crystalline phases present during glass formation. The result indicates that the incorporation of Ta_2O_5 did not cause any changes in the glass since only the amorphous halo in the range from 20 to 40° is observed.

The amount and type of crystalline phases obtained from the glassy systems are essential since they set the parameters for using glasses and/or glass ceramics. From the diffractogram of Fig. 3(b)–(d), the main crystalline phases present in all three glassy systems are combeite ($Na_6Ca_3Si_6O_{18}$) ICDD 98-002-1442 with a hexagonal crystalline structure and a secondary crystalline phase similar to apatite, known as silicorhenanite ($Na_2Ca_4(PO_4)_2SiO_4$) ICDD 032-1053 [26], which agrees well with the glass formulations since they are representative structures of silicates and phosphates vitreous network. Lefebvre et al. [30] pointed out that the orthophosphate ions in the glasses contribute to the crystallization of the silicorhenanite, while the diphosphate ions remain in the glass. On the other hand, in the formulations BG-0.1%Ta and BG-0.5%Ta, in addition to the crystalline phases of combeite and silicorhenanite, sodium tantalum phosphate ($NaTa(PO_4)_2$) JCPDS 038-0204 was detected. In the Raman spectra, it is inferred that the vibrations at 825 and 974 cm^{-1} are due to Ta—O bonds; these bands are more pronounced in BG-0.1%Ta, but the XRD reflections of sodium tantalum phosphate increase in intensity in BG-0.5%Ta due to the increase in the molar concentration of the glass formulation; the reduction in intensity of the silicorhenanite phase is associated with the extraction of phosphorous and sodium ions by the tantalum to crystallize into sodium tantalum phosphate. The formation of crystals of silicorhenanite and sodium tantalum phosphate increased the energy requirements verified with the ΔT, and in turn, an increase in both the T_c and T_m expressed by the K_H consistent with the nucleation and formation of new crystalline phases in the BG-0.1%Ta.

FTIR can detect and quantify local changes in the structural symmetry of glass. Fig. 4(a)–(c) presents the FTIR transmission spectra; the stretching bands at 495 cm^{-1} and bend at 788 cm^{-1} are associated with the Si—O—Si bending of silicate $[SiO_4]^{2-}$ group [32], silicate that is related to the BO units in silanol units as seen in Raman; the reflection at 924 cm^{-1} is identified as Si—NBO [33], it is observed in all glass formulations as well as the vibration in Raman at 945 cm^{-1} associated with

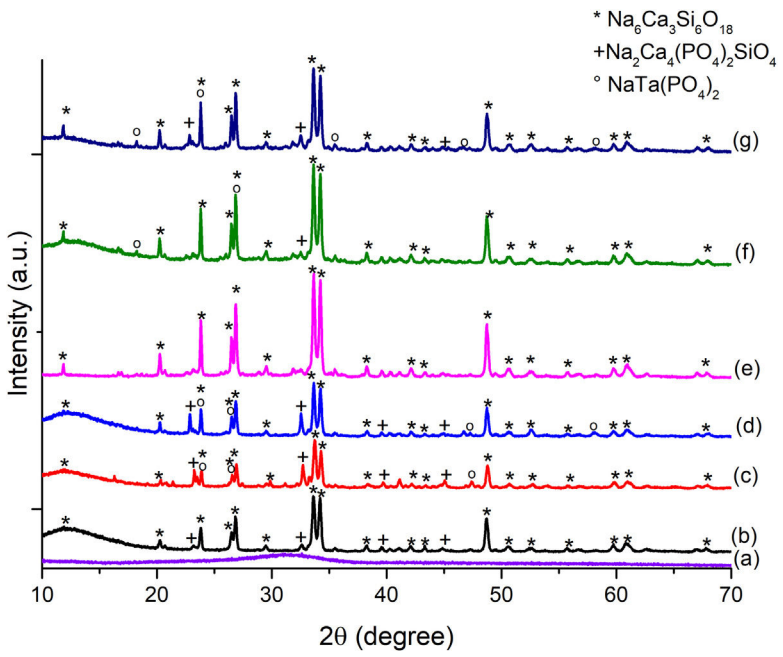

Fig. 3 – XRD diffractograms of bioglass powders heat-treated at 900 °C for 1 h, (a) BG0, (b) BG-0.1%Ta and (c) BG-0.5%Ta. Sintered bioglass scaffolds, (d) SBG0, (e) SBG-0.1%Ta and (f) SBG-0.5%Ta.

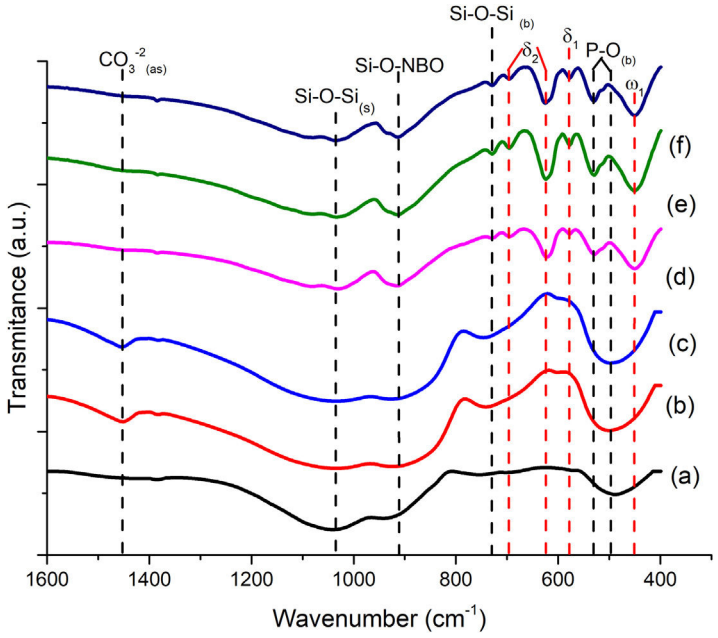

Fig. 4 – FTIR spectra for the glassy systems: (a) BG0, (b) BG-0.1%Ta, and (c) BG-0.5%Ta. Sintered bioglass scaffolds, (d) SBG0, (e) SBG-0.1%Ta and (f) SBG-0.5%Ta.

NBO units present in all formulations, and the 1041 cm^{-1} band represents the stretching Si—O—Si and which in turn overlaps with the asymmetric stretching PO_4^{-3} [34]; the asymmetric stretching band at 1454 cm^{-1} is related to the non-hydrolyzed species retained by the bases [29]. When Ta_2O_5 was incorporated, the main differences in the spectra were found in the PO_4^{-3} bend detected at 584 cm^{-1}, at 625 cm^{-1} Si—O—Si δ_2 (3-membered rings), and in turn, the amplitude in the 924 cm^{-1} mode up to 800 cm^{-1}, which correspond to vibration Si—NBO [34] that is associated with the incorporation of tantalum as part of the structure where it shares bonds with phosphorus to form sodium tantalum phosphate phase and consequently modifying the silicon lattice. The formation energy of the oxide of Ta is higher than that of Si; therefore, the Ta—Si reactivity is more likely than the Si—Si reaction [35].

Scaffold characterization

The results obtained for the physical properties are presented in Table 4; from these data, it is observed that the higher the tantalum oxide content, the lower the density and the higher the porosity and the surface area. The influence of incorporating Ta_2O_5 in the glass formulation was analyzed in the previous section, as this could modify the properties of the scaffold. As mentioned, the material's interconnectivity and porosity are essential for cell migration and adhesion without sacrificing its physical properties. It has been observed that the % shrinkage and the surface area are affected by heat treatments and the compressive strength, which decreases proportionally with the increase in the material's porosity.

The scaffolds' shrinkage percentage was determined since it directly influences the material's porosity and compressive strength. Table 4 also shows the shrinkage results for the scaffolds after heat treatment, highlighting the SBG-0.5%Ta formulation scaffolds that had 36.53% shrinkage, being the lowest shrinkage of the three formulations; in the second step of the scaffold fabrication, the resin is pyrolyzed, and the structure of the scaffold is fragile since it is supported only by the bioglass particles which in turn during sintering densified due to the exposure of the particles to high temperatures with the formation of necks and contraction of the material, reducing the axial dimensions of the structure and decreasing porosity. Regarding the density values, the BG-0.5%Ta powder density was 2.6463 g/cm^3, being the least dense and therefore the one that exhibited the most negligible contraction that agrees well with the 84.24% porosity presented in Table 4, which also is the highest porosity value compared to the other compositions; added to this, it had the highest surface area of 17.431 cm^2, considering that the surface area influences aspects such as the kinetics of the reactions. In this case, it is related to the available surface of the scaffold for cell adhesion.

The microporosity of the scaffolds was studied by SEM, and the micrographs are observed in Fig. 5. In the SBG0, Fig. 5(a), it can be observed that both walls and struts have a rough surface, which would enable the adhesion of cells; a micrograph at higher magnification of 350×, Fig. 5(d), shows an interconnected porosity with microporosity of the walls. The SBG-0.1%Ta is observed in Fig. 5(b), and it is an evident lower porosity with crystals on the walls of the scaffold; however, in Fig. 5(e), it is shown that pores are interconnected, which can allow filtration of biological fluids into the material. Fig. 5(c) shows the surface of the SBG-0.5%Ta; there are pores of various sizes with rough surfaces, and the interconnectivity can be better observed at higher magnification in Fig. 5(f). All undoped and doped scaffolds are expected to provide the ideal morphology for adhesion and cell proliferation on the surface and inside the material.

The samples' pore size and pore size distribution were evaluated from the SEM images taken for the undoped and doped 45S5 bioglass scaffolds at 100× and with the assistance of the Nano measurer 1.2 software. SBG0 had pore size distribution within the range of 30–218 μm, average pore size of 77.6 ± 13.86 μm (Feret), with 38% repeatability; on the other hand, the SBG-0.1%Ta presented pore size distribution in the range of 21–177 μm, average pore size of 57.11 ± 11.44 μm (Feret) with 33% repeatability; finally, in the SBG-0.5%Ta, pore size distribution were estimated in the range of 19–260 μm, average pore size of 78.06 ± 9.71 Feret μm) and 37% repeatability. Cell penetration is possible since the osteoblasts are approximately 20–30 μm in size [18] in scaffolds with a pore size of 100 μm [36]. As it is known, the particle size of glass powders (3.51–2.87 μm) is inversely proportional to the surface reactivity of the precursor (0.4052–0.5649 m^2/g) and, in turn, is directly proportional to the density (2.7117–2.6463 g/cm^3) so, during foaming, the formulation with higher Ta content presents more significant expansion due to the lower density of the precursors and a better contact area and when the material is consolidated the porosity is more open. It can be added that Liang et al. [37] analyzed the impact of particle size on scaffold formation and demonstrated that smaller particles exhibit more efficient packing with better pore size distribution. They emphasize that microporosity is controlled by the particle size and the processing of the material; as for nanopores, the conversion reaction governs their formation. The size of the pores of the three scaffold formulations will allow the exchange of body fluid within the structure and cell migration so that adhesion and cell proliferation may be achieved along with the formation of new bone.

Fig. 3(e)–(g) presents the XRD analysis performed on doped and undoped 45S5 bioglass scaffolds after sintering. The primary crystalline phase, combeite ($Na_6Ca_3Si_6\ O_{18}$) ICDD 98-002-1442 and silicorhenanite ($Na_2Ca_4(PO_4)_2SiO_4$) were identified, which agree with the results of the different heat-treated glass powders. Several authors report $Na_6Ca_3Si_6O_{18}$ [33,34], $Na_2Ca_2Si_3O_9$ [35], and $Na_2CaSi_2O_6$ [25,38] as the main crystalline phases in bioglass scaffolds, which are isostructures that change depending on the temperature at which they are treated and the size of the glass particle; being $Na_2Ca_2Si_3O_9$ the crystalline phase that predominates in treatments above 900 °C [26,39]. The reflections of this phase decreased in intensity as the amount of Ta_2O_5 increased. However, in scaffolds with Ta_2O_5, the presence of peaks at 18.35°, 23.83°, 35.55°, 46.65° and 57.99° is observed, which are associated with the sodium tantalum phosphate phase ($NaTa(PO_4)_2$) JCPDS 038-0204. The same crystalline phases were found in the heat-treated glassy powder systems. The size of the crystallites for the highest intensity peak ($2\theta \approx 33°$) was calculated from the Scherrer equation, $D = K\lambda/\beta\cos\theta$, where K is the Scherrer constant, λ is the wavelength of the X-ray, β is the full width at half maximum (FWHM) of the peak and θ is the Bragg angle. From the diffractograms in Fig. 3(e)–(g), the apparent size of the combeite crystals was determined to be 14.86, 14.37 and 13.79 (SBG0, SBG-0.1%Ta and SBG-0.5%Ta, respectively), a shift in the amplitude of the peak from 33.45°–33.99° (SBG0) to 33.43°–33.91°(SBG-0.5%Ta), is interpreted as a reduction in the size of the combeite crystal, Si and O rich phase, with the growth of silicorhenanite and sodium tantalum phosphate crystals, which are P rich phases; therefore, the particle or grain that is made up of one or more crystallites may have a greater surface area, as observed in Table 2, as the molar concentration of tantalum in the bioglass formulation increases.

The FTIR spectra for sintered scaffolds are shown in Fig. 4(d)–(f), where the change in vibration mode at 451 cm^{-1} associated with silicates $[SiO_4]^{2-}$ ω_1 (≥5 membered rings) is

Table 4 – Physical and mechanical properties for undoped and doped 45S5 bioglass sintered scaffolds.

Sample	$\rho_{app.}$ (g/cm^3)	Porosity (%)	SA (cm^2/g)	Shrinkage (%)	Compressive strength (MPa)	E (GPa)
SBG0	0.687 ± 0.041	74.890 ± 1.525	14.415 ± 0.273	50.04	1.40 ± 0.07	0.47 ± 0.19
SBG-0.1%Ta	0.544 ± 0.067	79.838 ± 2.489	16.101 ± 0.669	42.31	0.53 ± 0.27	0.18 ± 0.07
SBG-0.5%Ta	0.425 ± 0.027	84.242 ± 1.012	17.431 ± 0.846	36.53	0.42 ± 0.10	0.19 ± 0.16

SA = apparent surface area.

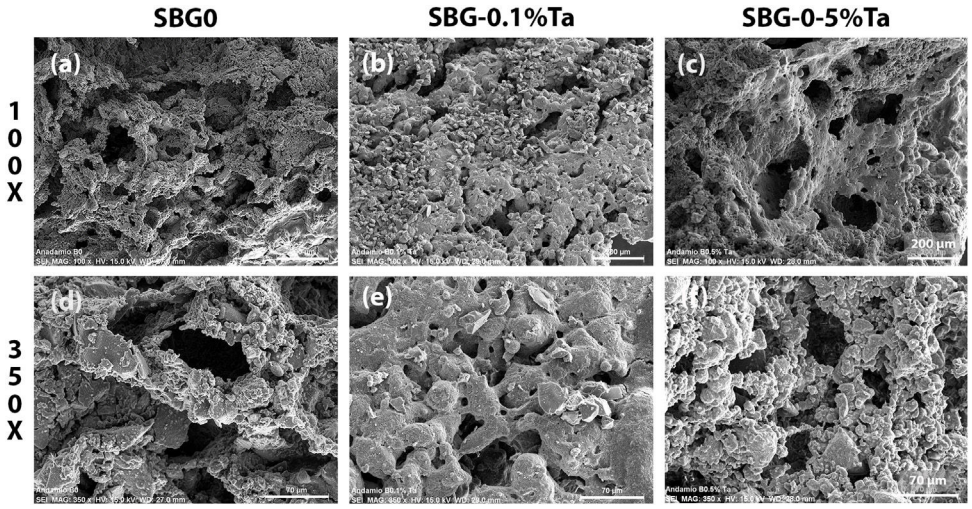

Fig. 5 – SEM images of the porous structure of undoped and doped bioglass scaffolds.

observed [32]; the bend at 530 cm^{-1} is associated with $PO_4{}^{-3}$, while 578 and 624 cm^{-1} with δ_1 and δ_2, respectively of Si—O—Si network, overlap the P—O link [32], due to the interaction of P_2O_5, as a BO former in the silicon network when crystallization occurs [29], which in turn, it can be seen with the silicorhenanite phase observed in the diffractogram, it is known that within the silicon network a silicon ion shares a bond with 4 silicon or phosphorus ions, for its part the phosphorus only shares 3 bridge bonds, since an oxygen ions shares a double bond with the phosphorus (P=O). This ion functions as NBO in the formation of polymerized anions. Still, it can be linked to cations in the network to form M—O—PO_3 bonds (M: Ca, K, Na, and Ta), which are developed in the scaffold manufacturing process during sintering; the 730 cm^{-1} band is identified as the Si—O—Si bending [34,38]; the vibration at 913 cm^{-1} is identified as Si—NBO [33,38], since the introduction of modifiers into the glass network can break Si—O—Si, Si—O—P, and P—O—P bonds, leading to depolymerization of the network with the detection of NBO's such as Si—O and P—O [26] and the band at 1036 cm^{-1} representative of the asymmetric extension Si—O—Si is observed [32]. The same band was observed in the as-melt-quenched glass, but with more significant bending and with a displacement of less than 20 cm^{-1}; this is due to the better interaction of the network-forming bridges after the heat treatment, which was already reported by Bretcanu et al. [40], subjecting glasses to low heating rates for prolonged times promotes crystallization. Note that after 800 cm^{-1} and 500 cm^{-1}, there is a widening in the bands associated with Si—NBO and P—O, respectively, as the molar concentration of Ta_2O_5 increases; this is attributed to the presence of the crystalline phase sodium tantalum phosphate and tantalum acting as a network modifier, reducing the crystallinity of the glass but, in turn, favoring the bioactivity of the material.

Fig. 6 shows HRTEM images for pulverized SBG-0.5%Ta sample. It can be observed that the three crystalline phases identified are in agreement with the XRD results; in Fig. 6(a), the combeite crystals, d = 2.53248 plane (015), are displayed with a shorter interplanar distance with respect to the silicorhenanite crystalline phases, Fig. 6(b), d = 2.812 plane (031), and the $NaTa(PO_4)_2$ phase, Fig. 6(c), d = 2.6100; as identified in the diffractograms when incorporating Ta_2O_5. The EDS analyses determined that the ratio Ca/Si = 0.713 is consistent with the values of the combeite crystals. Likewise the ratio Ca/Si = 5.710 corresponds to the silicorhenanite crystals, as well as the ratio Na/Ta = 0.127 for $NaTa(PO_4)_2$ crystals [41].

Mechanical characterization

Table 4 shows the average compressive strength of bioglass scaffolds without doping, and the scaffolds doped; it was determined that for the doped scaffolds there was a decrease in the compressive strength being more noticeable in SBG-0.5% Ta with a value of up to 0.42 MPa, which is consistent given the increase in porosity of the scaffolds, which is estimated at 84.24%. Meanwhile, the SBG-0.1% Ta had a compressive strength of 0.53 MPa. The E evaluates the increase in the deformation of the material concerning the tension

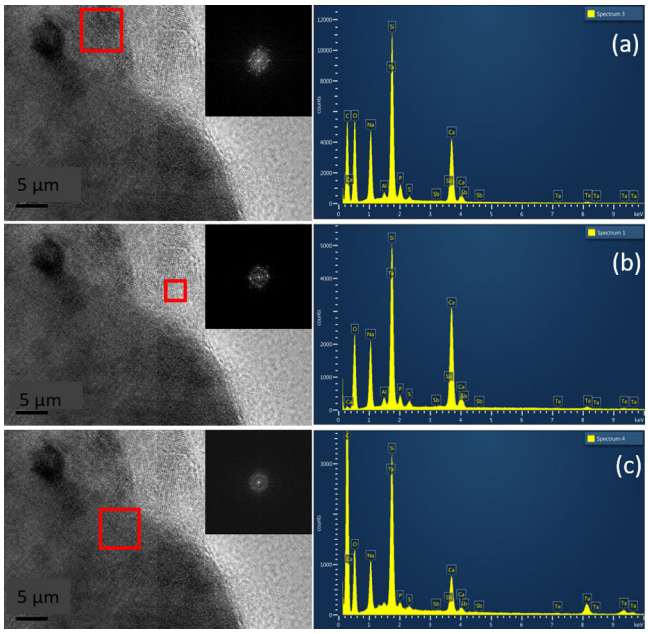

Fig. 6 – TEM micrographs of the pulverized SBG-0.5%Ta, the selected area for the FFT pattern (insert) is shown, and the three crystalline phases identified were (a) combeite ($Na_6Ca_3Si_6O_{18}$), (b) silicorhenanite ($Na_2Ca_4(PO_4)_2SiO_4$), and (c) sodium tantalum phosphate $NaTa(PO_4)_2$.

applied to the material. Trabecular or cancellous bone has a compressive strength that varies between 2 and 12 MPa and an *E* between 0.5 and 5 GPa [42]. Compressive strength and *E* are close to the lower limit for trabecular bone, and the scaffolds are intended to be used as temporary bone grafts to favor cell adhesion and proliferation and promote the formation of new bone matrix.

The values obtained in this study are representatively higher in terms of porosity and pore size ranges; however, their compressive strength values are low compared to those obtained by other synthesis routes (with lower porosity), but like those scaffolds obtained by sol–gel/template, freeze drying, solvent casting, and replica techniques. Du et al. [19] improved the porosity of silica-based scaffolds by doping with Mg and Mn since the incorporation of these ions modified the structure of the Si—O—Si network, forming new crystalline phases of magnesium and manganese silicates, which in turn changed the microstructure of the pore walls and consequently the compressive strength was reduced; also demonstrated that the sintering temperature can densify the scaffold walls and collapse the microporosity by shrinking the material. For their part, Gerhardt et al. [43] produced scaffolds by infiltration of poly(D,L lactide) (PDLLA) suspension with micro and nanoparticles of bioglass (BG); it is worth mentioning that the scaffolds with a smaller particle size of infiltrated BG did not improve the mechanical properties, but increased the porosity up to 91%, this associated with the reduced interfacial bond between PDLLA and BG caused by the increase in the specific surface area of the nanoparticles, limiting the resistance of the material to low applied stresses. The sintering temperature in powder technology plays a crucial role since it increases the crystallinity of the material and its densification, which can slow down the growth of hydroxyapatite on the surface of the material and its dissolution. Furthermore, the micropores collapse during sintering, the material shrinks, and the mechanical resistance increases [44]. The shrinkage level of the structure increases with increasing sintering temperature [25]. Doping the bioglass formulations with Ta_2O_5 produced a change in the microstructure and crystalline morphology of the material by increasing the crystalline phases, which led to lattice distortion by breaking silicon and phosphorous network to form phosphorous crystalline structures with tantalum, modifying the silicon network and consequently decreasing the compressive strength of the scaffolds with the increase in the amount of doped Ta ions [17,19].

Conclusions

Ta_2O_5-doped bioglass was successfully produced from melt-quenching and pulverized to obtain particle sizes of 3.51–2.87 µm; the density of BG0 (2.7117 g/cm^3) decreased (2.6463 g/cm^3) with the integration of Ta_2O_5. BG-0.1%Ta had the highest estimated values for ΔT, K_H, and K_W. The higher the K_H value, the greater the thermal stability and thus glass forming ability, that is, higher resistance of the glass to devitrification at heating, increasing T_c. In contrast, the T_c in BG-0.5%Ta was reduced by the presence of NBO due to Ta_2O_5 addition. For all formulations, $\Delta T \leq 100\,^{\circ}C$, so glasses exhibited open structures that favor bioactivity. By Raman and FTIR spectroscopies, $_{Si}Q^2$ species generated by NBO and P-O vibrations were identified, modifying the crystalline lattice of silicon in BG-0.1%Ta and BG-0.5%Ta, which in turn, developed the sodium tantalum phosphate phase that reduced the size of the combeite crystals present in all formulations while increasing the specific surface area to 0.5649 m^2/g in BG-0.5%Ta. These characteristics improve the physical properties of the doped glasses; with this, the pore size of scaffolds expanded to 19–260 µm, with an average of 78.05 ± 9.71 µm (Feret), and the porosity increased to 84% in SBG-0.5%Ta. The reduction in density led to the formation of microporosity in the walls of the scaffolds. The reactivity and density of the doped glasses and the sintering temperature during the scaffold manufacturing process reduced the compression resistance in proportion to that of undoped scaffolds. However, compression resistance values are close to that of trabecular bone and favor their use as temporary implants for bone tissue regeneration. It is proposed as future work to analyze the effect of doping on the bioactivity of the scaffolds, and subsequently carry out in vitro and in vivo tests.

Funding

This work was supported by the National Council of Science and Technology, Mexico, CONACYT [Project CB-2013-C01-222262], and the Coordinación de la Investigación Científica of the Universidad Michoacana de San Nicolás de Hidalgo.

Conflict of interest

The authors declare that they have no known competing financial interests or personal relationships that could have influenced the work reported in this paper.

Acknowledgments

This work was supported by the National Council of Science and Technology, Mexico, CONACYT [Project CB-2013-C01-222262], and the Coordinación de la Investigación Científica of the Universidad Michoacana de San Nicolás de Hidalgo. The authors acknowledge CONACYT for the generous scholarship provided to Cindy Sinaí Velázquez-González.

The authors thank the Geochemistry Department, Geology Institute, UNAM, for XRF analyses, and the Central Microscopy Laboratory, Physics Institute, UNAM for TEM analysis.

REFERENCES

1 J.R. Jones, Bioactive glass as synthetic bone grafts and scaffolds for tissue engineering, in: J.R. Jones, A.G. Clare (Eds.), Bioglasses: an introduction, John Wiley & Sons, Ltd., Chichester, 2012, pp. 177–201, http://dx.doi.org/10.1002/9781118346457.
2 A. Flores-Jacobo, E.A. Aguilar-Reyes, C.A. León-Patiño, Effect of dopants on the physical, mechanical, and biological properties of porous scaffolds for bone tissue engineering, Biomed. Mater. Dev. (2022), http://dx.doi.org/10.1007/s44174-022-00020-5.
3 B.M. Lovelock, J.E. Porterfield, Blood clotting: the function of electrolytes and of calcium, Biochem. J. 50 (1952) 415–420, http://dx.doi.org/10.1042/bj0500415.
4 F. Baino, S. Fiorilli, C. Vitale-Brovarone, Bioactive glass-based materials with hierarchical porosity for medical applications: review of recent advances, Acta Biomater. 42 (2016) 18–32, http://dx.doi.org/10.1016/j.actbio.2016.06.033.
5 S. Pourshahrestani, E. Zeimaran, N.A. Kadri, N. Gargiulo, S. Samuel, S.V. Vaveen, T. Kamarul, M.R. Towler, Gallium-containing mesoporous bioactive glass with potent hemostatic activity and antibacterial efficacy, J. Mater. Chem. B 4 (2016) 71–86, http://dx.doi.org/10.1039/C5TB02062J.
6 C. Persson, L. Guadalini, F. Baruffaldi, L. Pierotti, M. Baleani, Radiopacity of tantalum-loaded acrylic bone cement, P.I. Mech. Eng. H: J. Eng. Med. 220 (2006) 787–791, http://dx.doi.org/10.1243/09544119JEIM88.
7 J.J. Schmidt, J. Rowley, H.J. Kong, Hydrogels used for cell-based drug delivery, J. Biomed. Mater. Res. Part A 87A (2008) 1113–1122, http://dx.doi.org/10.1002/jbm.a.32287.
8 V.K. Balla, S. Banerjee, S. Bose, A. Bandyopadhyay, Direct laser processing of a tantalum coating on titanium for bone replacement structures, Acta Biomater. 6 (2010) 2329–2334, http://dx.doi.org/10.1016/j.actbio.2009.11.021.
9 J.D. Bobyn, G.J. Stackpool, S.A. Hacking, M. Tanzer, J.J. Krygier, Characteristics of bone ingrowth and interface mechanics of a new porous tantalum biomaterial, J. Bone Joint Surg. Br. 81-B (1999) 907–914, http://dx.doi.org/10.1302/0301-620X.81B5.0810907.
10 T. Miyaza, H.-M. Kim, T. Kokubo, C. Ohtsuki, H. Kato, T. Nakamura, Mechanism of bonelike apatite formation on bioactive tantalum metal in a simulated body fluid, Biomaterials 23 (2002) 827–832, http://dx.doi.org/10.1016/S0142-9612(01)00188-0.
11 A. Mendoca, M.S. Rahman, A. Alhalawani, O. Rodríguez, R.C. Gallant, H. Ni, O.M. Clarkin, M. Towler, The effect of tantalum incorporation on the physical and chemical properties of ternary silicon–calcium–phosphorous mesoporous bioactive glasses, J. Biomed. Mater. Res. Part B 107 (2018) 2229–2237, http://dx.doi.org/10.1002/jbm.b.34310.
12 E. Fiume, E. Verné, F. Baino, Crystallization behavior of SiO_2–P_2O_5–CaO–MgO–Na_2O–K_2O bioactive glass powder, Biomed. Glasses 5 (2019) 46–52, http://dx.doi.org/10.1515/bglass-2019-0004.
13 M. Grellier, L. Bordenave, L. Amédée, Cell-to-cell communication between osteogenic and endothelial lineages: implications for tissue engineering, Trends Biotechnol. 27 (2009) 562–571, http://dx.doi.org/10.1016/j.tibtech.2009.07.001.
14 L. Nair, C. Laurencin, Biodegradable polymers as biomaterials, Prog. Polym. Sci. 32 (2007) 762–798, http://dx.doi.org/10.1016/j.progpolymsci.2007.05.017.
15 D.K. Pattanayak, B.T. Rao, T.R. Rama Mohan, Calcium phosphate bioceramics and bioceramic composites, J. Sol–Gel Sci. Technol. 59 (2010) 432–447, http://dx.doi.org/10.1007/s10971-010-2354-y.
16 V. Miguez-Pacheco, T. Büttner, A.L.B. Maçon, J.R. Jones, T. Fey, D. de Ligny, P. Greil, J. Chevalier, A. Malchere, A.R. Boccaccini, Development and characterization of lithium-releasing silicate bioactive glasses and their scaffolds for bone repair, J. Non-Cryst. Solids 432 (2016) 65–72, http://dx.doi.org/10.1016/j.jnoncrysol.2015.03.027.
17 J. Li, C. Zhao, C. Liu, Z. Wang, Z. Ling, B. Lin, B. Tan, L. Zhou, Y. Chen, D. Liu, X. Zou, W. Liu, Cobalt-doped bioceramics scaffolds fabricated by 3D printing show enhanced osteogenic and angiogenic properties for bone repair, BioMed. Eng. OnLine 20 (2021) 1–24, http://dx.doi.org/10.1186/s12938-021-00907-2.
18 R. Zhao, C. Siyu, W. Zhao, L. Yang, B. Yuan, V.S. Ioan, A. Iulian, X. Yang, X. Zhu, X. Zhang, A bioceramic scaffold composed of strontium-doped three-dimensional hydroxyapatite whiskers for enhanced bone regeneration in osteoporotic defects, Theranostics 10 (2020) 1572–1589, http://dx.doi.org/10.7150/thno.40103.
19 Z. Du, H. Leng, L. Guo, Y. Huang, T. Zheng, Z. Zhao, X. Liu, X. Zhang, Q. Cai, X. Yang, Calcium silicate scaffolds promoting bone regeneration via the doping of Mg^{2+} or Mn^{2+} ion, Compos. Part B-Eng. 190 (2020) 107937, http://dx.doi.org/10.1016/j.compositesb.2020.107937.
20 E. Aguilar-Reyes, C. León-Patiño, B. Jacinto-Diaz, L.-P. Lefebvre, Structural characterization and mechanical evaluation of bioactive glass 45S5 foams obtained by a powder technology approach, J. Am. Ceram. Soc. 12 (2012) 3776–3780, http://dx.doi.org/10.1111/j.1551-2916.2012.05465.x.
21 P. Sepulveda, A.H. Bressiani, J. Bressiani, L. Meseguer, J.B. Konig, In vivo evaluation of hydroxyapatite foams, J. Biomed. Mater. Res. 62 (2002) 587–592, http://dx.doi.org/10.1002/jbm.10173.
22 A. Tilocca, A. Cormack, Structural effects of phosphorus inclusion in bioactive silicate glasses, J. Phys. Chem. B 111 (2007) 14256–14264, http://dx.doi.org/10.1021/jp075677o.
23 L. de Siqueira, T.M.B. Campos, S.E.A. Camargo, G.P. Thim, E.S. Trichês, Structural, crystallization and cytocompatibility evaluation of the 45S5 bioglass-derived glass-ceramic containing niobium, J. Non-Cryst. Solids 555 (2021) 120629, http://dx.doi.org/10.1016/j.jnoncrysol.2020.120629.
24 M.D. O'Donnell, P.L. Candarlioglu, C.A. Miller, Materials characterization and cytotoxic assessment of strontium-substituted bioactive glasses for bone regeneration, J. Mater. Chem. 20 (2010) 8934–8941, http://dx.doi.org/10.1039/C0JM01139H.

25 R. Kumar, S.A. Kumar, K.P. Bhuvana, Preparation and evaluation of bioactivity of porous bioglass tablets for bone tissue regeneration, SciMed. J. 1 (2019) 112–123, http://dx.doi.org/10.28991/SciMEdJ-2019-0103-1.

26 A. Baranowska, M. Lésniak, M. Kochanowicz, J. Zmojda, P. Miluski, D. Dorosz, Crystallization kinetics and structural properties of the 45S5 bioactive glass and glass-ceramic fiber doped with Eu^{3+}, Materials 13 (2020) 1281, http://dx.doi.org/10.3390/ma13061281.

27 M. Monisha, M.S. Murari, M.I. Sayyed, H. Al-Ghamdi, A.H. Almuqrin, G. Lakshminarayana, S.D. Kamath, Thermal, structural and optical behaviour of Eu^{3+} ions in zinc alumino boro-silicate glasses for bright red emissions, Mater. Chem. Phys. 270 (2021) 124787, http://dx.doi.org/10.1016/j.matchemphys.2021.124787.

28 R. Madeeha, Z. Rehana, F. Farah, B. Farooq, H. Tousif, Characterization, bioactivity and antimicrobial properties of a metal-ceramic composite for bone regeneration, Ceram. Int. 46 (2020) 16663–16669, http://dx.doi.org/10.1016/j.ceramint.2020.03.239.

29 M.S. Araujo, A.C. Silva, J.F. Bartolomé, S. Mallo-Castanho, Structural and thermal behavior of 45S5 Bioglass®-based compositions containing alumina and strontium, J. Am. Ceram. Soc. 103 (2020) 3620–3630, http://dx.doi.org/10.1111/jace.17061.

30 L. Lefebvre, J. Chevalier, L. Gremillard, R. Zenati, G. Thollet, D. Bernache-Assolant, A. Govin, Structural transformations of bioactive glass 45S5 with thermal treatments, Acta Mater. 55 (2007) 3305–3313, http://dx.doi.org/10.1016/j.actamat.2007.01.029.

31 H. Aguiar, J. Serra, P. González, B. León, Structural study of sol-gel silicate glasses by IR and Raman spectroscopies, J. Non-Cryst. Solids 355 (2009) 475–480, http://dx.doi.org/10.1016/j.jnoncrysol.2009.01.010.

32 G. Socrates, Infrared and Raman Characteristic Group Frequencies, 3rd ed., John Wiley & Sons, Ltd., Chichester, 2001.

33 A.T. Shah, Q. Ain, A.A. Chaudhry, A.F. Khan, B. Iqbal, S. Ahmad, S.A. Siddiqi, I.U. Rehman, A study of the effect of precursor on physical and biological properties of mesoporous bioactive glass, J. Mater. Sci. 50 (2015) 1794–1804, http://dx.doi.org/10.1007/s10853-014-8742-x.

34 G.M. de Pietro, C. Pereira, R.R. Gonçalves, S.J.L. Ribeiro, C.D. Freschi, F.C. Cassanjes, G. Poirier, Thermal, structural, and crystallization properties of new tantalum alkali-germanate glasses, J. Am. Ceram. Soc. 98 (2015) 2086–2093, http://dx.doi.org/10.1111/jace.13555.

35 A.M.F. Alhalawani, M.R. Towler, The effect of $ZnO–Ta_2O_5$ substitution on the structural and the thermal properties of $SiO_2–ZnO–SrO–CaO–P_2O_5$ glasses, Mater. Charact. 114 (2016) 218–224, http://dx.doi.org/10.1016/j.matchar.2016.03.004.

36 M. Kamath, S. Ahmed, M. Dhanasekaran, S. Winkins, Polycaprolactone scaffold engineered for sustained release of resveratrol: therapeutic enhancement in bone tissue engineering, Int. J. Nanomed. 9 (2014) 183–195, http://dx.doi.org/10.2147/IJN.S49460.

37 W. Liang, Y. Tu, H. Zhou, C. Liu, C. Rüssel, Borophosphate glass-ceramic scaffolds by a sodium silicate bonding process, J. Non-Cryst. Solids 357 (2011) 958–962, http://dx.doi.org/10.1016/j.jnoncrysol.2010.07.068.

38 I. Hammami, S.R. Gavinho, A.S. Pádua, I. Sá-Nogueria, J.C. Silva, J.P. Borges, M.A. Valente, M.P.F. Graça, Bioactive glass modified with zirconium incorporation for dental implant applications: fabrication, structural, electrical, and biological analysis, Int. J. Mol. Sci. 24 (2023) 10571, http://dx.doi.org/10.3390/ijms241310571.

39 A.R. Boccaccini, Q. Chen, L. Lefebvre, L. Gremillard, J. Chevalier, Sintering crystallisation and biodegradation behaviour of Bioglass®-derived glass-ceramics, Faraday Discuss. 136 (2007) 27–44, http://dx.doi.org/10.1039/B616539G.

40 O. Bretcanu, X. Chatzistavrou, K. Paraskevopoulos, R. Conradt, I. Thompson, A.R. Boccaccini, Sintering and crystallisation of 45S5 Bioglass® powder, J. Eur. Ceram. Soc. 29 (2009) 3299–3306, http://dx.doi.org/10.1016/j.jeurceramsoc.2009.06.035.

41 B. Cabal, L. Alou, F. Cafini, R. Couceiro, D. Sevillano, L. Esteban-Tejeda, F. Guitián, R. Torrecillas, J.S. Moya, A new biocompatible and antibacterial phosphate free glass-ceramic for medical applications, Sci. Rep. 4 (2014) 5440, http://dx.doi.org/10.1038/srep05440.

42 Q. Fu, Bioactive glass scaffolds for bone tissue engineering, in: G. Kaur (Ed.), Biomedical Therapeutic and Clinical Applications of Bioactive Glasses, Woodhead Publishing, Duxford, 2019, pp. 417–442, http://dx.doi.org/10.1016/B978-0-08-102196-5.00015-X.

43 L.C. Gerhardt, K.L. Widdows, M.M. Erol, C.W. Burch, J.A. Sanz-Herrera, I. Ochoa, R. Stämpfli, I.S. Roqan, S. Gabe, T. Ansari, A.R. Boccaccini, The pro-angiogenic properties of multi-functional bioactive glass composite scaffolds, Biomaterials 32 (2011) 4096–4108, http://dx.doi.org/10.1016/j.biomaterials.2011.02.032.

44 E.A. Aguilar-Reyes, C.A. Leon-Patiño, E. Villicaña-Molina, V.I. Andrés, L.-P. Lefebvre, Processing and in vitro bioactivity of high-strength 45S5 glass-ceramic scaffolds for bone regeneration, Ceram. Int. 3 (2017) 6868–6875, http://dx.doi.org/10.1016/j.ceramint.2017.02.107.